Numerical investigation of the compressible flow past an aerofoil

LI-WEI CHEN, CHANG-YUE XU and XI-YUN LU†

Department of Modern Mechanics, University of Science and Technology of China,
Hefei, Anhui 230026, China

Numerical investigation of the compressible flow past an 18 % thick circular-arc aerofoil was carried out using detached-eddy simulation for a free-stream Mach number $M_\infty = 0.76$ and a Reynolds number $Re = 1.1 \times 10^7$. Results have been validated carefully against experimental data. Various fundamental mechanisms dictating the intricate flow phenomena, including moving shock wave behaviours, turbulent boundary layer characteristics, kinematics of coherent structures and dynamical processes in flow evolution, have been studied systematically. A feedback model is developed to predict the self-sustained shock wave motions repeated alternately along the upper and lower surfaces of the aerofoil, which is a key issue associated with the complex flow phenomena. Based on the moving shock wave characteristics, three typical flow regimes are classified as attached boundary layer, moving shock wave/turbulent boundary layer interaction and intermittent boundary layer separation. The turbulent statistical quantities have been analysed in detail, and different behaviours are found in the three flow regimes. Some quantities, e.g. pressure-dilatation correlation and dilatational dissipation, have exhibited that the compressibility effect is enhanced because of the shock wave/boundary layer interaction. Further, the kinematics of coherent vortical structures and the dynamical processes in flow evolution are analysed. The speed of downstream-propagating pressure waves in the separated boundary layer is consistent with the convection speed of the coherent vortical structures. The multi-layer structures of the separated shear layer and the moving shock wave are reasonably captured using the instantaneous Lamb vector divergence and curl, and the underlying dynamical processes are clarified. In addition, the proper orthogonal decomposition analysis of the fluctuating pressure field illustrates that the dominated modes are associated with the moving shock waves and the separated shear layers in the trailing-edge region. The results obtained in this study provide physical insight into the understanding of the mechanisms relevant to this complex flow.

Key words: boundary layers, compressible, simulation

---

1. Introduction

Owing to the obvious importance in a wide range of fundamentals and applications, a great effort has been made in the past decades to study the compressible flow in transonic regime past an aerofoil. Self-sustained shock wave motions on aerofoils are associated with the phenomenon of buffeting, and the shock-induced fluctuations are particularly severe. Comprehensive reviews on this subject have been given by

† Email address for correspondence: xlu@ustc.edu.cn

Tijdeman & Seebass (1980) and Lee (2001). The physical mechanisms of the shock motion are not yet fully understood, even though some work has been performed over the last 50 years (Lee 2001). Moving shock wave/turbulent boundary layer interaction is also responsible for important flow phenomena, e.g. unsteady boundary layer separation and vortex shedding in the trailing-edge region, which are major causes of broadband noise (Wang, Freund & Lele 2006). Thus, various fundamental mechanisms dictating the complex flow characteristics, such as moving shock wave behaviours, turbulent boundary layer characteristics, kinematics of coherent structures and dynamical processes in flow evolution, are still completely unclear and are of great interest for future detailed studies.

Self-sustained shock wave motions on aerofoils have been investigated experimentally and numerically (e.g. Lee 2001 and the references therein). Tijdeman & Seebass (1980) have classified the shock wave motions as being of three types, i.e. type A, B and C. Previous experimental studies of transonic flow over an 18 % thick circular-arc aerofoil at zero incidence have indicated that upstream-propagating shock waves occur alternately on the upper and lower surfaces for a certain range of the free-stream Mach number (McDevitt, Levy & Deiwert 1976; Levy 1978; McDevitt 1979; Marvin, Levy & Seegmiller 1980), which belongs to type C. Moreover, some numerical simulations have been performed using the time-dependent two-dimensional Reynolds-averaged Navier–Stokes (RANS) equations with turbulence models (e.g. Marvin *et al.* 1980; Rumsey *et al.* 1996; Xiao, Tsai & Liu 2003). A zonal detached-eddy simulation (DES) method has also been used to predict the buffet phenomenon on a supercritical aerofoil (Deck 2005). Those simulations have analysed the shock wave motion and the evolution of shock-induced separation. In particular, Lee (Lee 1990; Lee, Murty & Jiang 1994) has given an explanation of the mechanism of self-sustained shock oscillation and proposed a feedback model to estimate the frequency of oscillation for the type A shock motion. Recently, global-stability theory has been used to predict shock-induced transonic-buffet onset on aerofoils based on steady solutions of the two-dimensional RANS equations, and the theoretically predicted results for the onset of flow unsteadiness agree well with experiments and unsteady calculations (Crouch, Garbaruk & Travin 2007; Crouch *et al.* 2009).

The interaction between the sustained moving shock wave and turbulent boundary layer along the aerofoil surface is an important issue in understanding the flow characteristics. Smits & Dussauge (1996) have classified the shock wave/turbulent boundary layer interactions as compression corner interactions or incident shock interactions. Numerical investigations have been performed for the compression corner interactions (e.g. Loginov, Adams & Zheltovodov 2006; Ringuette, Wu & Martín 2008) or incident shock interactions (e.g. Teramoto 2005; Pirozzoli & Grasso 2006). Andreopoulos, Agui & Briassulis (2000) have analysed several types of shock/turbulence interactions and concluded that in the case of wall-bounded interactions the shock system is highly unsteady. Correspondingly, the flow considered here involves complex interaction phenomena and turbulent boundary layer behaviours associated with the shock wave motion and the surface curvature of the aerofoil. The relevant study comparably is scarce.

The interaction between a shock wave and turbulence is mutual. Since the 1950s, linear interaction analyses (LIA) on turbulence modification by the shock wave have been performed with an emphasis on the acoustic wave generation behind the shock wave (e.g. Ribner 1953, 1954, 1987; Lee, Lele & Moin 1997). Through the linear analyses, it is found that turbulent fluctuations are amplified across the

shock wave, and significant acoustic noise is also generated because of the interaction of vortical turbulence with the shock wave. Jacquin, Cambon & Blin (1993) have applied homogeneous rapid distortion theory (RDT) to deal with shock/turbulence interaction and found that RDT is inappropriate for the analysis of shock/turbulence interaction, since the shock front curvature and unsteadiness cannot be accounted for in the analysis. Lele (1992) has formulated the exact jump relations across a shock in turbulent mean flow and has analytically indicated that the mean propagation speed of a shock wave that brings about a specified compression is slightly faster than its classical value. The idealized shock waves/turbulence interactions have been reviewed by Andreopoulos *et al.* (2000). Those investigations indicate that turbulence amplification through shock wave interaction is a direct effect of the Rankine–Hugoniot relations.

The turbulent boundary layer separation induced by the sustained moving shock wave and the evolution of coherent vortical structures in the trailing-edge region play an important role in overall flow behaviours. Characterizing the kinematics of coherent structures and dynamical processes in flow evolution is still one of the fundamental challenges in fluid mechanics. Usually, dynamical evolutions are analysed by the proper orthogonal decomposition (POD; Lumley 1967; Berkooz, Holmes & Lumley 1993) and stochastic estimation (Adrian & Moin 1988) methods, and coherent vortical structures are often discussed relative to the importance of vortices (e.g. Robinson 1991; Jeong & Hussain 1995; Chakraborty, Balachandar & Adrian 2005). On the other hand, the Lamb vector acts as a vortex force, and its character plays an important role in establishing the nature of the flow (Truesdell 1954; Wu, Ma & Zhou 2006). The Lamb vector divergence and curl are associated with the momentum and vorticity transport in flow field (Wu *et al.* 2006) and may construct a rigorous methodology for the study of what are generically referred to as coherent structures or motions (Hamman, Klewicki & Kirby 2008). Recently, the mathematical properties and physical interpretations of the Lamb vector divergence that substantiate its kinematical and dynamical significance have been analysed by Hamman *et al.* (2008).

As the flow considered here has a high Reynolds number $Re \sim O(10^7)$ (McDevitt *et al.* 1976; Levy 1978; Marvin *et al.* 1980), the methodology used is a significant issue in numerical simulations. Recent advances in the DES have provided a powerful tool for studying high-Reynolds-number flows and have comprehensively been surveyed by Spalart (2009). In order to deal with high-Reynolds-number and massively separated flows, the DES was first proposed by Spalart *et al.* (1997) and is convincingly more capable presently than either the RANS simulation or large-eddy simulation (LES; Spalart 2009 and references therein). Further, as an example, extensive work by means of the DES and its extensions has been performed in Sagaut's group (e.g. Mary & Sagaut 2002; Deck 2005; Sagaut, Deck & Terracol 2006; Simon *et al.* 2007) and has confirmed that the DES is a reliable way to study the high-Reynolds-number flows.

The present work investigates the compressible flow past an 18 % thick circular-arc aerofoil for a free-stream Mach number $M_\infty = 0.76$ and a Reynolds number $Re = 1.1 \times 10^7$, corresponding to experiments (McDevitt *et al.* 1976; Levy 1978; McDevitt 1979; Marvin *et al.* 1980). The three-dimensional Favre-averaged compressible Navier–Stokes equations are solved numerically by means of a finite-volume approach (Lu *et al.* 2005) combined with shock capture technique (Hill, Pantano & Pullin 2006). The DES is implemented for turbulence closure. Results have been validated against the experimental data. The motivation of this work is to study various fundamental mechanisms dictating the complex flow phenomena.

This paper is organized as follows. The mathematical formulation and numerical method are briefly presented in §2. The computational overview and validation are described in §3. Detailed results are then given in §4 and the concluding remarks in §5.

2. Mathematical formulation and numerical method

2.1. *Governing equations and turbulence modelling*

To investigate the compressible flow past an aerofoil, the three-dimensional Favre-averaged compressible Navier–Stokes equations in generalized coordinates are employed. The equation of state for an ideal gas is used, and the molecular viscosity is assumed to obey Sutherland's law. To non-dimensionalize the equations, we use the free-stream variables including the density ρ_∞, temperature T_∞, speed of sound a_∞ and chord of the aerofoil c as characteristic scales. A detailed description of the mathematical formulation can be found in our previous paper (e.g. Lu *et al.* 2005).

The initial and boundary conditions are presented as follows. The initial condition is set as the free-stream quantities. The far-field boundary conditions are treated by local one-dimensional Riemann-invariants. No-slip and adiabatic conditions are applied on the aerofoil surface. Periodic condition is used in the spanwise direction of the aerofoil.

The DES is implemented in the present work for turbulence closure (Spalart *et al.* 1997). The model is derived from the Spalart–Allmaras model (Spalart & Allmaras 1992), which is a one-equation model for the eddy viscosity $\tilde{v}$ by solving a transport equation. The reader may refer to the original paper (Spalart & Allmaras 1992) for details on the constants and the quantities involved.

The model is provided with a destruction term for the eddy viscosity that depends on the distance to the nearest solid wall d. This term adjusts the eddy viscosity $\tilde{v}$ to scale with local deformation rate $\tilde{S}$ producing an eddy viscosity given by $\tilde{v} \sim \tilde{S}d^2$. Spalart *et al.* (1997) proposed to replace d to the closest wall with $\tilde{d}$ defined by

$$\tilde{d} = \min(d, C_{DES}\,\Delta), \qquad (2.1)$$

where Δ represents a characteristic mesh length and is defined as the largest of the spacings in all three directions, i.e. $\Delta = \max(\Delta x, \Delta y, \Delta z)$, and the constant C_{DES} is taken as 0.65 from a calibration of the model for isotropic turbulence (Shur *et al.* 1999). We have followed the detailed analysis of the numerical treatments indicated by Sagaut *et al.* (2006) and carefully examined the present simulations.

2.2. *Numerical procedure*

The governing equations are numerically solved by the finite-volume method. The temporal integration is performed using an implicit approximate-factorization method with sub-iterations to ensure the second-order accuracy (Simon *et al.* 2007). Both the convective and diffusive terms are discretized with second-order centred schemes, and a fourth-order low artificial numerical dissipation is employed to prevent numerical oscillations at high wavenumbers (Lu *et al.* 2005; Wang *et al.* 2007). To minimize numerical contaminations, special attention has been paid to the numerical dissipation, and the coefficient of the dissipation term was carefully selected as $\epsilon_4 = 0.003$, which is small enough to ensure the physical dissipation. Similar to our previous test (Lu *et al.* 2005), the spatial accuracy and the relevant numerical dissipation were assessed by considering a benchmark problem of decaying isotropic turbulence. We have
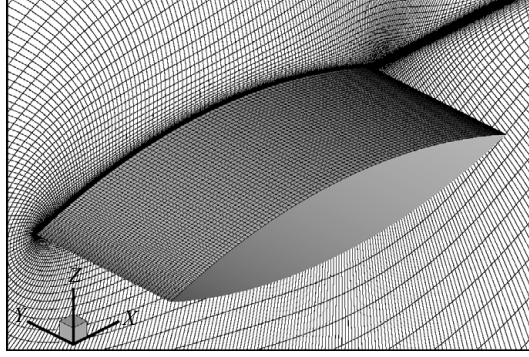
FIGURE 1. The computational mesh plotted by three-interval nodes in each direction.

identified that the numerical viscosity is smaller than the subgrid-scale viscosity term provided by the DES.

To capture the discontinuity caused by shock wave, a second-order upwind scheme with the Roe's flux-difference splitting is introduced into the inviscid flux. The artificial dissipation is also turned off in the region in which the upwind scheme works. A binary sensor function $\Phi_{i+1/2}$ at cell face $i + 1/2$ is used for the detection of shock waves; $\Phi_{i+1/2}$ is determined by the pressure and density curvature criteria proposed by Hill *et al.* (2006),

$$\alpha_p^{i+1/2} = \max\left(\alpha_p^i, \alpha_p^{i+1}\right), \quad \alpha_\rho^{i+1/2} = \max\left(\alpha_\rho^i, \alpha_\rho^{i+1}\right) \tag{2.2}$$

and

$$\alpha_p^i = \left|\frac{p_{i+1} - 2p_i + p_{i-1}}{p_{i+1} + 2p_i + p_{i-1}}\right|, \quad \alpha_\rho^i = \left|\frac{\rho_{i+1} - 2\rho_i + \rho_{i-1}}{\rho_{i+1} + 2\rho_i + \rho_{i-1}}\right|, \tag{2.3}$$

where α_p^i and α_ρ^i represent the pressure and density relative curvatures at cell centre, respectively. When $\alpha_p^{i+1/2} > c_1$ and $\alpha_\rho^{i+1/2} > c_2$, $\Phi_{i+1/2}$ is 1; but zero, otherwise. The three-dimensional version of this detection is used in the simulations. Similar to the treatment (Hill *et al.* 2006), the values of c_1 and c_2 that proved to give the best results are chosen as 0.01. Based on this detection, the Roe's second-order upwind flux only operates at the cells in the vicinity of shock waves.

3. Computational overview and validation

3.1. *Computation overview*

We consider a compressible flow past an 18 % thick circular-arc aerofoil at zero incidence with the free-stream Mach number $M_\infty = 0.76$ and the Reynolds number based on the chord of the aerofoil equal to 1.1×10^7. The selected parameters are the same as those performed in experiments (e.g. McDevitt *et al.* 1976; Levy 1978; Marvin *et al.* 1980). The relevant experimental data will thus be employed to validate the present calculation.

The grid generation is an important issue in the DES, since the grid extension is related to the resolved wavelengths and the eddy viscosity level (Spalart 2001, 2009; Deck 2005). As plotted in figure 1, the grids are of C type with a far-field boundary at $40c$ away from the aerofoil in the (x, z) plane, and grid stretching is employed to increase the grid resolutions near the surface and in the wake region. As the spanwise

Grid	N_{xz}	N_y	$\Delta z_{min}/c$	Δz^+	$a_\infty \Delta t/c$	St
Grid 1	262×128	32	5×10^{-6}	~ 2	0.005	0.125
					0.002	0.139
					0.001	0.146
Grid 2	392×160	42	3×10^{-6}	~ 1	0.005	0.132
					0.002	0.145
					0.001	0.147
Grid 3	522×192	42	2×10^{-6}	<1	0.005	0.135
					0.002	0.146
					0.001	0.148
Grid 4	392×160	62	3×10^{-6}	~ 1	0.002	0.148
					0.001	0.148
Grid 5	522×192	62	2×10^{-6}	<1	0.002	0.148
					0.001	0.148
Grid 6	522×192	82	2×10^{-6}	<1	0.002	0.148
					0.001	0.148

TABLE 1. Validation of grid resolution and time step.

domain is usually set as at least twice the thickness of the aerofoil (Sagaut *et al.* 2002; Deck 2005), the spanwise length is thus chosen as $0.4c$ and divided uniformly.

To assess the effects of grid resolution and time step on the calculated results, six typical grids denoted by grids 1–6 and three time steps with main characteristics are listed in table 1. Detailed comparisons of the calculated results using different computational conditions will be given in the following subsection. Our *a posteriori* verifications show that there are at least 40 nodes in the vorticity thickness over the surface in the attached boundary layer region. Moreover, following the suggestion of Spalart (2001), the grid cells are close to cubic in the LES region.

The present code is equipped with a multi-block domain decomposition feature to facilitate parallel processing in a distributed computing environment (Lu *et al.* 2005). The present computational domain is divided into 32 sub-domains for parallel processing. The computed time elapses to about $400c/a_\infty$ to obtain statistically meaningful turbulence properties in the temporal average operation.

Based on the time-dependent resolved density $\bar{\rho}$, pressure $\bar{p}$, temperature $\tilde{T}$ and velocity $\tilde{u}_i$, where a tilde denotes the Favre filter, several averaging operations will be needed. To clearly present the post-process, some symbols used in this paper are introduced as follows: $\langle \rangle$ means the average in time (after careful elimination of the transient part of their time-dependent variations) and in the spanwise direction, and $\{\phi\} = \langle \bar{\rho}\phi \rangle / \langle \bar{\rho} \rangle$ with a variable ϕ. Then, their fluctuations are obtained as (Garnier, Sagaut & Deville 2002) $\rho' = \bar{\rho} - \langle \bar{\rho} \rangle$, $p' = \bar{p} - \langle \bar{p} \rangle$, $T'' = \tilde{T} - \{\tilde{T}\}$ and $u_i'' = \tilde{u}_i - \{\tilde{u}_i\}$, respectively.

3.2. *Validation*

To validate the present simulation, we compare numerical results and experimental data (McDevitt *et al.* 1976; McDevitt 1979; Marvin *et al.* 1980) in terms of the frequency of shock motion, averaged pressure coefficient, mean velocity and turbulent shear stress, as well as some quantities related to the shock wave motion, which will be shown in the following section.
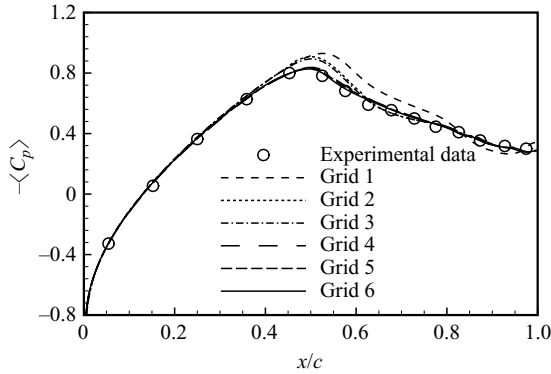
FIGURE 2. Distribution of time-averaged pressure coefficient. The lines using grids 1–6 represent computational result, and the symbol represents experimental data (McDevitt *et al.* 1976). The parameters of grids 1–6 are listed in table 1.

Assessments of the effect of time step are performed on the calculated solutions. The frequency values (St) of shock wave motion for various runs are exhibited in table 1. The smaller the time step, the more accurately the frequency value can be determined. Detailed discussion on the frequency will be given in §4.1.2. Based on our careful examinations, the time step $0.001c/a_\infty$ can provide reliable results and will be used in the present simulation.

Figure 2 shows the profile of average pressure $\langle C_p \rangle$ coefficient. The pressure distribution is somewhat affected by the grid resolution in the separation region, and it is exhibited that the results with grids 4–6 compare favourably with the experimental data (McDevitt *et al.* 1976). Figure 3 shows the transverse distributions of the averaged streamwise velocity and shear stress at the measurement locations from $x/c = 0.8$ to $x/c = 1.05$, where z^* is the relative transverse coordinate defined as $z^* = z - z_s$ with z_s being the transverse location of the aerofoil surface. Reasonable agreement is obtained with the experimental measurements of Marvin *et al.* (1980) using grids 4–6 and time step $\Delta t = 0.001c/a_\infty$. To make the prediction accurate, the results given below were calculated by the finest grid, grid 6.

Moreover, figure 4 shows the profiles of the ensemble-averaged velocity, turbulent kinetic energy and shear stress from conditionally sampled data with the averaging interval of $0.01c/a_\infty$, similar to the treatment used by Marvin *et al.* (1980). These results are calculated using grid 6 and $\Delta t = 0.001c/a_\infty$. It is seen that the variations during one cycle compare reasonably with the experimental data (Marvin *et al.* 1980).

On the other hand, the resolved energy spectrum obtained by grid 6 and $\Delta t = 0.001c/a_\infty$ is shown in figure 5. The resolved scales seem to reach an inertial sub-range, reasonably close to $St^{-5/3}$ scaling (Kawai & Fujii 2005). The spatial spectrum can be approximately obtained using Taylor's hypothesis which is limited to homogeneous turbulence with small turbulence intensity (Pope 2000). The illustrated slope indicates that the present calculation may reliably simulate the energy cascade behaviour (e.g. Kawai & Fujii 2005; Wang *et al.* 2007). Based on the grid sensitivity study and the resolved energy spectrum analysis, it is ensured that grid 6 has an adequate mesh resolution to simulate essential features of the flow.

Further, the present numerical strategy has already been applied with success to a wide range of turbulent flows such as the compressible turbulent swirling flows injected into a co-axial dump chamber (Lu *et al.* 2005) and compressible flows over
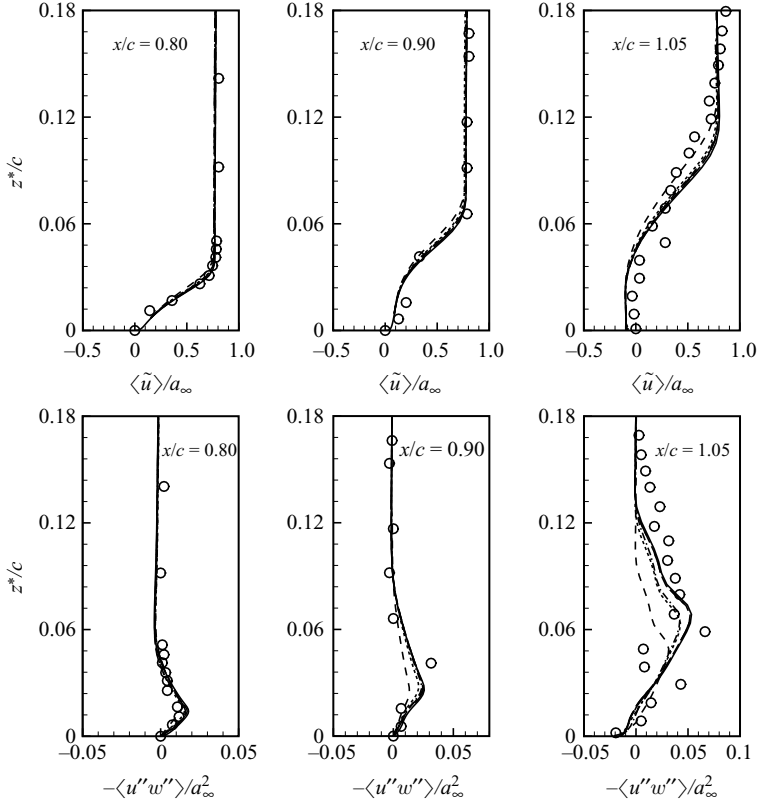
FIGURE 3. Transverse distributions of mean streamwise velocity and shear stress obtained numerically and experimentally, where the lines using grids 1–6 represent computational results with the same legends as those in figure 2, and the symbol denotes experimental data (Marvin *et al.* 1980). Here, z^* is the relative transverse coordinate defined as $z^* = z - z_s$ with z_s being the transverse location of the aerofoil surface.

a circular cylinder (Xu, Chen & Lu 2009). We have carefully examined the physical model and numerical approach used in this study and have verified that the calculated results are reliable. Thus, the present simulation will now be used to obtain a better insight into the physical mechanisms underlying the flow considered.

4. Results and discussion

4.1. *Flow structures and moving shock wave behaviours*

4.1.1. *Flow structures*

The present flow field involves an array of intricate phenomena, e.g. self-sustained shock wave motion, shock wave and turbulent boundary layer interaction and boundary layer separation induced by the shock wave (Tijdeman & Seebass 1980; Lee 2001). To assess the existence of coherent structures in the flow field, figure 6 shows an instantaneous snapshot of flow field depicted by isosurface of the Q criterion (Jeong & Hussain 1995),

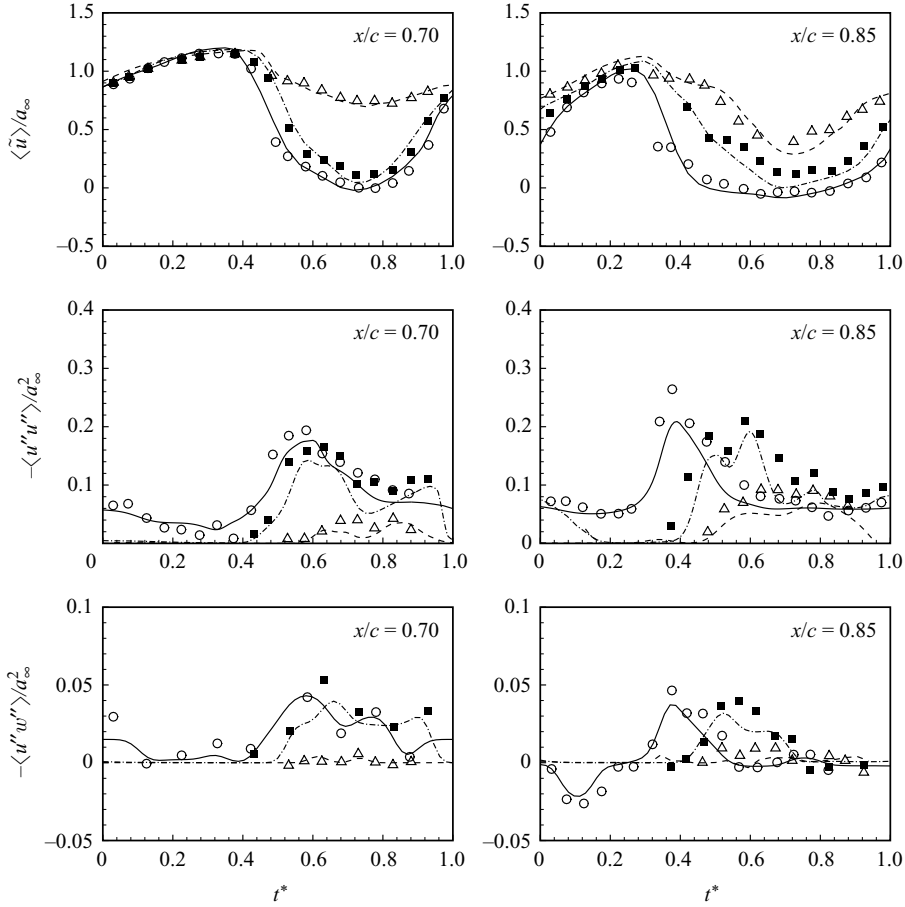$$Q = -\frac{1}{2}(\|\mathbf{S}\|^2 - \|\mathbf{\Omega}\|^2), \tag{4.1}$$

FIGURE 4. Comparison of time histories of velocity, turbulent kinetic energy and shear stress with the experimental data (Marvin *et al.* 1980). At $x/c = 0.70$ (left column), the solid, dashdotted and dashed lines denote the present results at $y/c = 0.084$, 0.090 and 0.100, respectively, and the symbols $\bigcirc$, $\blacksquar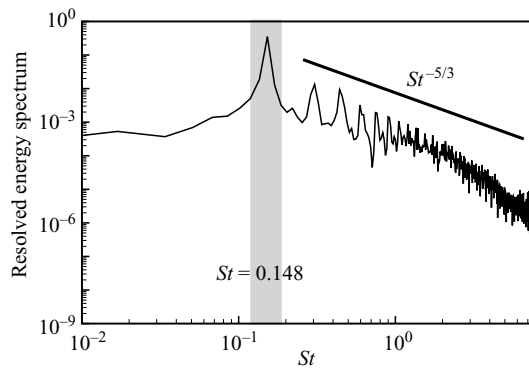e$ and $\triangle$ denote the corresponding experimental data. At $x/c = 0.85$ (right column), the solid, dash-dotted and dashed lines denote the present results at $y/c = 0.055$, 0.075, and 0.100, respectively, and the symbols $\bigcirc$, $\blacksquare$ and $\triangle$ denote the corresponding experimental data.

FIGURE 5. Resolved energy spectrum at the location ($x/c = 0.95$, $y/c = -0.2$ and $z/c = 0.2$) calculated by grid 6 and $\Delta t = 0.001 c/a_\infty$.
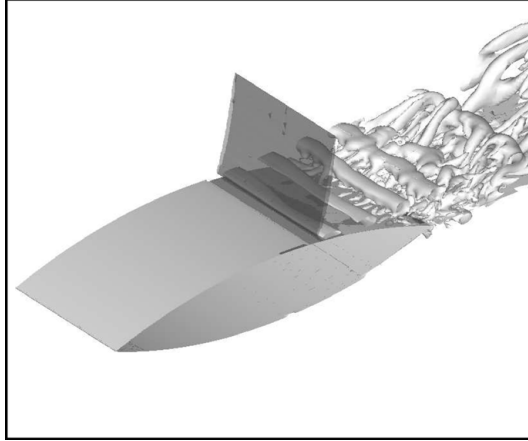
FIGURE 6. Isosurface of the Q criterion ($Q = 10(U_\infty/c)^2$). The surface of shock wave is exhibited by the isosurface of $\|\nabla\bar{\rho}\| = 10(\rho_\infty/c)$.

where $\boldsymbol{S}$ and $\boldsymbol{\Omega}$ denote the strain and the rotation tensor, respectively. A positive value of Q presents the regions in which the rotation exceeds the strain. The shock wave shape is reasonably visualized in figure 6 by the isosurface of density gradient. It is identified that the deformation of shock wave shape along the spanwise direction is negligibly small even near the turbulent boundary layer. Moreover, the boundary layer separation induced by the moving shock wave occurs. The separated free shear layer rolls up and becomes the three-dimensional complex structures because of the vortical instability as the shear layer evolves downstream. The streamwise vortical structures become strengthened in the near wake.

To illustrate the unsteady features of the flow, figure 7 shows the time development of flow structures using the isocontours of $\|\nabla\bar{\rho}\|$, for clarity, in the mid-span (x, z) plane. The numerical schlieren-like visualizations agree well with experimental shadowgraphs showing the unsteady flow field (McDevitt *et al.* 1976; Marvin *et al.* 1980). Here, we pay attention on flow evolution over the upper surface. A series of compression waves develop in the region near the trailing edge and move upstream to coalesce into a strong shock wave at $x/c = 0.83$ approximately. This shock wave moves upstream while increasing its strength and induces the boundary layer separation. Then, the shock wave weakens again to be weak shock wave or compression wave around the mid-chord. Further, the compression wave continues its upstream motion, leaves the aerofoil from the leading edge and propagates upstream into the oncoming flow. Meanwhile, the compression wave diffraction at the top of shock wave reasonably occurs. As a symmetrical aerofoil is considered, this phenomenon is repeated alternately between the upper and lower surfaces.

4.1.2. *Shock wave motion*

From the preceding description of the shock wave evolution, it is reasonably identified that the shock wave motion belongs to type C classified by Tijdeman & Seebass (1980), which is also confirmed by the previous experiments (McDevitt *et al.* 1976; Levy 1978; McDevitt 1979; Marvin *et al.* 1980). To determine the frequency of shock wave motion, figure 8 shows the power spectrum of the time-dependent lift force exerted on the aerofoil. The primary frequency corresponding to the highest peak is $St = 0.148$ approximately, or the reduced frequency, which is usually used in
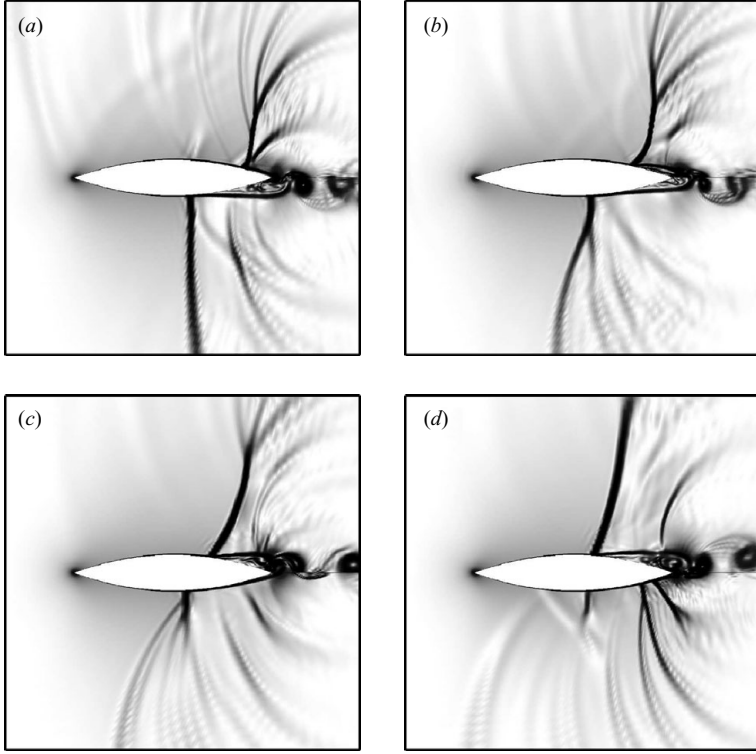
FIGURE 7. Numerical schlieren-like visualization by contours of $\|\nabla\bar{\rho}\|$ in the mid-span (x, z) plane during half-period with the same time increment from (a) to (d).
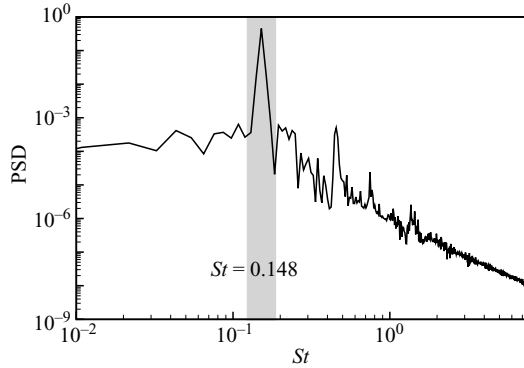

FIGURE 8. Power spectral density (PSD) of the time-dependent lift coefficient.

this problem (Tijdeman & Seebass 1980; Lee 2001), $k = \pi St \approx 0.465$, consistent with the previous experimental data, namely 0.44–0.49 (e.g. McDevitt *et al.* 1976; Levy 1978; Marvin *et al.* 1980). Since the frequency is greatly sensitive to the grid resolution and time step (Rumsey *et al.* 1996), the agreement between the numerical result and the previous experimental data also verifies the reliability of the present simulation as described above.

The location of shock wave motion along the surface is shown in figure 9(a), where t^* represents the fractional cyclic time during one period, and $t^* = 0$ is taken as the
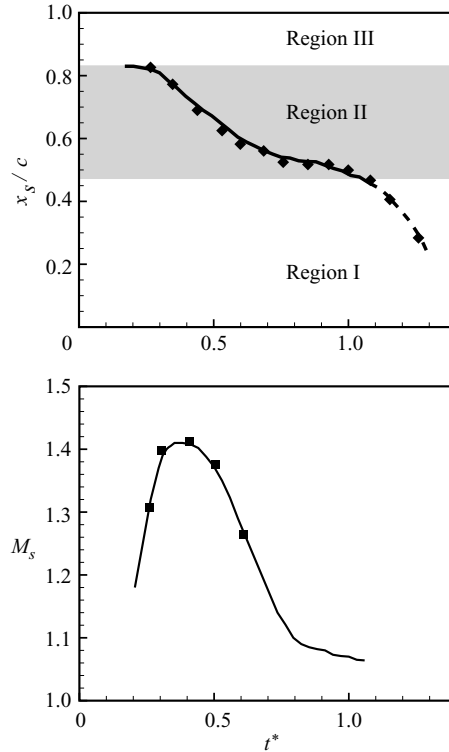
FIGURE 9. Shock wave location and Mach number ahead of shock wave. (*a*) Variation of shock wave location, where the solid (shock wave) and dashed (compression wave) lines represent computational result and the symbol represents experimental data (McDevitt 1979). Region I denotes attached boundary layer, region II denotes moving shock wave/turbulent boundary layer interaction; and region III denotes intermittent boundary layer separation. (*b*) Mach number ahead of shock wave, where the solid line and the symbol respectively represent computational result and experimental data (Marvin *et al.* 1980).

time when the shock wave is at the mid-chord of the aerofoil (McDevitt *et al.* 1976). Reasonable agreement is obtained with the experimental measurements (McDevitt 1979). As the shock wave moves upstream as shown in figure 7, the shock wave weakens and even becomes a compression wave, represented by the dashed line in figure 9(*a*). When the compression wave propagates upstream further and leaves the aerofoil from the leading edge, it is difficult to identify the compression wave position, which is not seen for $x/c < 0.2$ in figure 9(*a*). In addition, figure 9(*b*) shows the Mach number ahead of shock wave in a reference of shock-fixed frame. The values of M_s reach as high as 1.4, compared with the experimental data (Marvin *et al.* 1980).

4.1.3. *Feedback model of shock wave motion*

To understand the mechanism associated with the shock wave motion described above, we further discuss the feedback model for predicting the period of shock wave motion. A possible mechanism of self-sustained shock oscillation for type A during transonic buffeting with separated flow was first proposed by Lee (Lee 1990; Lee *et al.* 1994). The classification of the type A shock motion by Tijdeman & Seebass (1980) states that the shock moves almost sinusoidally and exists during the complete cycle of oscillation even though its strength varies. We will try to extend this feedback model to the present type C shock wave motion.

In the type A motion, a shock wave is oscillating on the upper surface of a supercritical aerofoil (Tijdeman & Seebass 1980). Lee proposed that the formed pressure waves propagate downstream in the separated flow region over the aerofoil at speed V_d, and the disturbances generate upstream-moving waves at speed V_u as the waves reach the trailing edge (Lee 1990; Lee *et al.* 1994). Further, Lee assumed that the period of shock oscillation is comparable with the time it takes for a disturbance to propagate from the shock to the trailing edge plus the duration for an upstream-propagating wave to reach the shock from the trailing edge in the outside region of the separated flow.

After careful examination of the flow evolution and comparison with previous results (e.g. Lee 1990; Xiao, Tsai & Liu 2006), we notice that there exist two typical differences between the present type C and the type A shock wave motion. As a symmetrical aerofoil is considered, unlike only an oscillating shock wave on the upper surface of a supercritical aerofoil (Lee 1990; Xiao *et al.* 2006), the upstream-propagating shock waves occur alternately between the upper and lower surfaces. The period of shock wave motion in this problem is referred to as the complete process of both the shock waves propagating upstream and leaving the aerofoil, as shown in figure 7. Thus, the period is twice that for the shock wave motion on one side surface. On the other hand, the feedback model proposed by Lee (Lee 1990; Lee *et al.* 1994) assumes that the flow behind the shock wave is fully separated and that the pressure waves induced by the shock wave propagate downstream in the separated flow region over the aerofoil. As shown in figures 7(*c*) and 7(*d*), the upstream-propagating shock wave does induce the boundary layer separation on the upper surface, while the flow remains attached to the lower surface, which results in the non-existence of downstream-propagating waves. In a mean sense, we thus assume that the mean speed over a complete period is taken as a half-speed of downstream-propagating pressure waves in the separated flow region over the aerofoil.

Based on the above analysis, we may reasonably give a feedback model for the type C shock wave motion through the idea of Lee (1990) to describe one complete period of shock wave motion as

$$T = 2[(c - \bar{x}_s)/V_d + (c - \bar{x}_s)/V_u], \tag{4.2}$$

where $\bar{x}_s$ denotes the mean location of the shock wave on the surface; V_u is the speed of upstream-propagating disturbances in the outside region of boundary layer; and V_d is the mean speed of downstream-propagating pressure waves.

The mean location of shock wave can be obtained more precisely with a statistical analysis in terms of the skewness factor of pressure fluctuation (Deck 2005), which is defined as $S_p = \langle p'^3 \rangle / \langle p'^2 \rangle^{3/2}$. The distribution of the skewness is shown in figure 10. The profile exhibits the positive and negative peaks with their locations $x/c = 0.47$ and $x/c = 0.83$, respectively. From the analysis (Deck 2005) and the flow evolution shown in figure 7, the shock wave motion along the aerofoil is characterized in the region of approximately $0.47 < x/c < 0.83$. Similar to the treatment for determining the mean location $\bar{x}_s$ (Girard 1999; Deck 2005), one can obtain that $\bar{x}_s$ corresponds to the abscissa between the positive and negative peaks where $S_p = 0$ or approximately $\bar{x}_s/c = 0.66$.

The speed of upstream-propagating disturbances is described as (Tijdeman 1977; Lee 1990)

$$V_u = (1 - M_{loc})a_{loc}, \quad M_{loc} = R[M_s - M_\infty] + M_\infty, \tag{4.3}$$
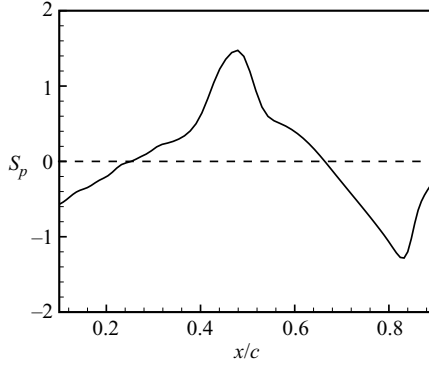
FIGURE 10. Distribution of the skewness of pressure fluctuation along the surface.

where a_{loc} is the local speed of sound; M_s is the Mach number at the surface; and R is a relaxation factor and was experimentally determined as 0.7 (Tijdeman 1977). This equation can be reasonably simplified as (Deck 2005)

$$V_u = (1 - M_\infty)a_{loc}. \tag{4.4}$$

Using the data predicted here, we can obtain that $V_u = 0.24U_\infty$ approximately. The speed of downstream-propagating pressure waves can be obtained from the cross-correlation analysis on pressure signals in the separated boundary layer and is calculated as $0.34U_\infty$, which will be determined in detail in § 4.3.1. Following the analysis described above, we can reasonably have $V_d = 0.17U_\infty$.

Finally, we apply (4.2) to obtain $T = 6.83c/U_\infty$ approximately or the non-dimensional frequency of the feedback loop $St \approx 0.146$, which agrees well with the frequency value 0.148 issued from the spectral analysis shown in figure 8. It means that the feedback model (4.2) may reliably predict the shock motion. Moreover, Crouch *et al.* (2007, 2009) advocated that transonic buffet results from the global instability, where the unsteadiness is characterized by phase-locked oscillations of the shock and the separated shear layer. In this situation, both the upper and lower surfaces of the aerofoil are responsible for the instability, consistent with the present model.

In addition, the expended feedback model (4.2) with reliable prediction also supports Lee's analysis (Lee 1990; Lee *et al.* 1994) and is helpful in understanding the physical mechanisms on the self-sustained shock wave motion. As shown in figure 7, the upstream-propagating pressure waves are generated by the impingement of large-scale structures on the surface of the aerofoil, interact with the shock wave and impart energy to maintain its motion on the surface. Moreover, this kind of feedback (Ho & Nosseir 1981) is typical of flows with self-sustained motions, such as flows over cavities (e.g. Heller & Delfs 1996; Larchevêque *et al.* 2003).

4.2. *Turbulent boundary layer characteristics*

4.2.1. *Division of flow regions*

The moving shock wave over the aerofoil surface exhibits substantial unsteadiness and deformation as a result of the interaction, whereas the turbulent quantities change considerably (Andreopoulos *et al.* 2000). Thus, another objective of this study is to investigate turbulent boundary layer characteristics.

In the shock wave/turbulent boundary layer interactions, e.g. compression corner interactions or incident shock interactions, the location of shock wave varies in a relatively small region, while the shock wave motion considered here occurs in a
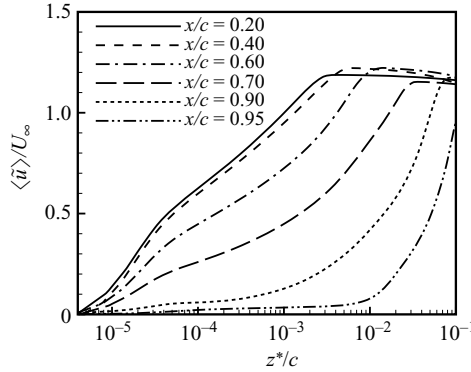
FIGURE 11. Distributions of mean streamwise velocity at various streamwise locations.

wide region along the surface. Based on our careful examination of the results, the shock wave motion is characterized in the region of approximately $0.47 < x/c < 0.83$. Moreover, as shown in figures $7(c)$ and $7(d)$, the upstream-propagating shock wave induces the boundary layer separation on the upper surface, while the flow remains attachment on the lower surface. This phenomenon is repeated alternately between the upper and lower surfaces. Thus, the flow over the aerofoil near the trailing edge is featured as intermittent boundary layer separation.

To clearly present the physical mechanisms involved in this flow, we may classify three typical flow regions, namely attached boundary layer (expressed as region I), moving shock wave/turbulent boundary layer interaction (region II) and intermittent boundary layer separation (region III). The regions along the aerofoil surface are shown schematically in figure $9(a)$. The attached and intermittently separated boundary layer regions lie from the leading edge to $x/c = 0.47$ and from $x/c = 0.83$ to the trailing edge, respectively.

In this section, we will discuss and compare the turbulent boundary layer characteristics in those three regions in terms of mean velocity, turbulence intensities, turbulent kinetic energy, pressure power spectra and the relevant turbulent quantities. Moreover, some topics related to compressibility effects on turbulence (Lele 1994), such as the turbulence Mach number, pressure dilatation correlation and dilatational dissipation, are also analysed.

4.2.2. *Mean velocity profiles*

The comparison of the mean streamwise velocity predicted numerically with experimental data (Marvin *et al.* 1980) has been shown in figure 3, and reasonable agreement is found. To deal with the mean velocity profiles in different regions, figure 11 shows the transverse distributions of the mean streamwise velocity. In region I, i.e. $x/c = 0.2$ and 0.4, we identify that the van-Driest-transformed mean velocity profiles, obtained as defined by Bradshaw (1977) and scaled by the wall-friction velocity, agree well with the linear and logarithmic law of the wall. In region II, i.e. $x/c = 0.6$ and 0.7, owing to the shock wave/boundary layer interaction, the velocity profiles exhibit a linear behaviour approximately in the viscous sublayer and no longer obey the logarithmic law. As the boundary layer separation occurs intermittently in region III, the mean streamwise velocity exhibits a small value in the near region of the surface. The flow characteristics associated with the boundary layer separation will be discussed in detail in §4.3.
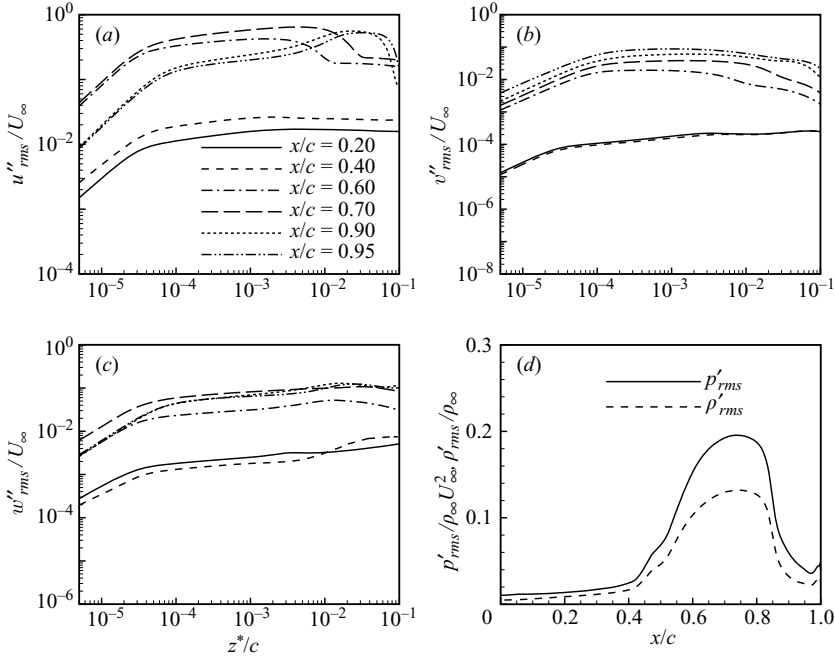
FIGURE 12. Distributions of turbulence intensities at various streamwise locations for the (a) streamwise, (b) spanwise and (c) transverse components and of (d) pressure and density fluctuations along the surface.

4.2.3. *Turbulence intensities*

Figure 12 shows the transverse distributions of the normalized turbulence intensity components. The streamwise component shown in figure 12(a) dominates the turbulence intensity as expected, compared with the other two components in figures 12(b) and 12(c). This character is consistent with measurements (Marvin *et al.* 1980). Here, we mainly pay attention to the behaviours in the three flow regimes.

As shown in figures 12(a)–12(c), the turbulence intensities in region II, such as at $x/c = 0.6$ and 0.7, are significantly enhanced compared with those at $x/c = 0.2$ and 0.4, consistent with the experimental measurements (Marvin *et al.* 1980) and theoretical predictions by LIA (Ribner 1953, 1954, 1987; Lee *et al.* 1997). Here, we introduce the turbulence Mach number defined as $M_t = \{u_i'' u_i''\}^{1/2}/a_{loc}$ (Lele 1992) and have identified that M_t reaches as high as approximately 0.5 in region II. Thus, the effect of the moving shock wave on turbulence intensities must be considered. As the turbulent normal stress is increased across a shock, the propagation speed of the shock wave becomes slightly faster to bring about a specified compression based on the shock-jump relations in a turbulent flow (Lele 1992). This specified compression is an additional mechanism that enhances the turbulence intensities in region II, compared with the compression corner shock interactions (Loginov *et al.* 2006) and incident shock interactions (Pirozzoli & Grasso 2006).

We further discuss the turbulence intensities in region III, as shown in figures 12(a)–12(c) at $x/c = 0.9$ and 0.95. Compared with region II, the streamwise turbulence intensity component near the surface reduces as shown in figure 12(a), and the spanwise component is somewhat enhanced as shown in figure 12(b). This behaviour is associated with the development of vortical structures over the surface. As shown in
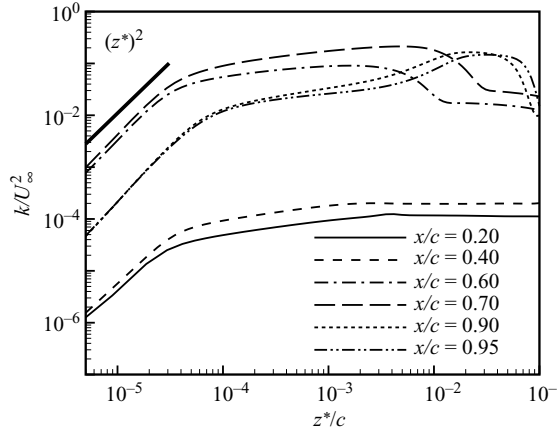
FIGURE 13. Distribution of specific turbulent kinetic energy at various streamwise locations.

figure 6, the separated shear layer induced by shock wave rolls up. Then, the spanwise vortical structures become unstable and the streamwise vortices strengthen gradually, resulting in the enhancement of the spanwise velocity fluctuation.

The distributions of the normalized pressure and density fluctuations along the surface are also shown in figure 12(*d*). The fluctuations are significantly enhanced in region II, consistent with the turbulence intensities. The profiles exhibit a sharp change at approximately $x/c = 0.83$, corresponding to the initial shock wave location coalesced by a series of upstream-propagating compression waves from the trailing-edge region shown in figure 7.

4.2.4. *Turbulent kinetic energy*

The distributions of the specific turbulent kinetic energy, i.e. $k = \{u_i'' u_i''\}/2$, are shown in figure 13. As noticed in the incident shock wave/boundary layer interaction (Pirozzoli & Grasso 2006), a spatially evolving turbulent compressible boundary layer exhibits similarities with the incompressible case. The turbulent kinetic energy for incompressible boundary layers obeys the near-wall asymptotic behaviour (Patel, Rodi & Scheuerer 1985; Speziale, Abid & Anderson 1992),

$$k \simeq A_k z^{*2}, \tag{4.5}$$

where A_k is a constant. We thus examine the near-wall asymptotic behaviour shown in figure 13 and find that the profiles satisfy (4.5) well in the viscous sublayer. The turbulent flow in the three regions exhibits similar asymptotic behaviour with different values of the constant A_k; a large value of A_k occurs in region II. Downstream of the interaction region, turbulence satisfies the asymptotic consistency with different values of the constant A_k and experiences a relaxation towards an equilibrium state.

Figure 14 shows the isocontour lines of the specific turbulent kinetic energy and turbulent shear stress $\tau_{xz} = -\{u''w''\}$. The specific turbulent kinetic energy has its maximum value around 0.25 inside the boundary layer in region II, which is associated with the mean velocity gradient, as discussed below, based on the budget terms in the turbulent kinetic energy transport equation. Correspondingly, the specific turbulent shear stress also reaches its maximum value around 0.1. To examine the shear effect and compressible effect on the turbulent characteristics, detailed discussion on the turbulent dissipation rate will be given below.
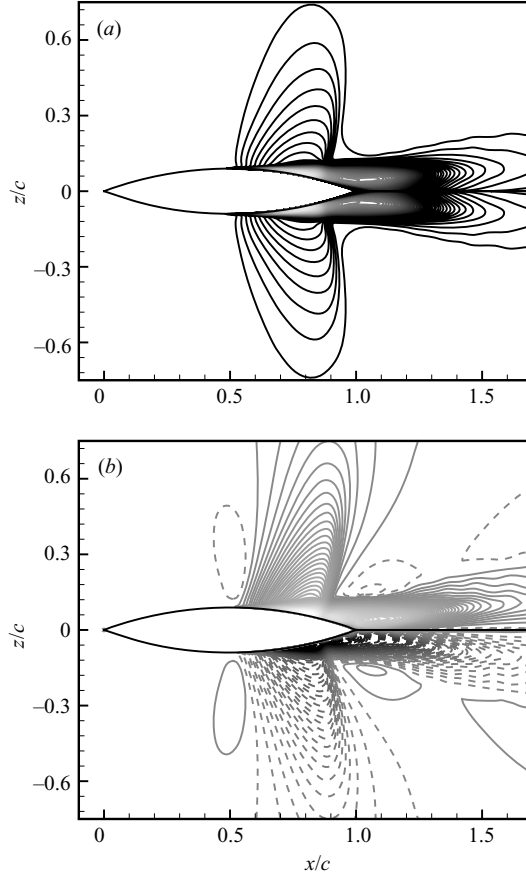
FIGURE 14. Contours of turbulent kinetic energy and shear stress: (*a*) turbulent kinetic energy with the contour levels between 0.005 (dark) and $0.3U_\infty^2$ (bright) and (*b*) turbulent shear stress with the contour levels between -0.1 (dark, dashed lines) and $0.1U_\infty^2$ (bright, solid lines).

We further discuss the structure parameter, defined as the ratio of the shear stress to the trace of the stress tensor $\tau_{xz}/2k$, which may be used for Reynolds stress closure (Herrin & Dutton 1997). Based on our careful examination of the structure parameters, we can understand that the turbulent shear and normal stresses undergo a different amplification mechanism over the aerofoil. In region II, the structure parameter varies approximately from 0.04 at $x/c = 0.47$ to 0.2 at $x/c = 0.83$ inside the boundary layer, while it exhibits a maximum value of about 0.4 outside the boundary layer, which may mainly be associated with the shock wave motion. In region III and in the near wake, the structure parameter along the shear layer changes from 0.2 at approximately $x/c = 0.83$ to 0.15 in the near wake, which agrees well with the values of structure parameter for the compressible shear layers (Harsha & Lee 1970; Simon *et al.* 2007).

4.2.5. *Budget terms in the turbulent kinetic energy transport equation*

The budget terms in the turbulent kinetic energy transport equation, which have been normalized by the free-stream velocity and given in detail by Shyy & Krishnamurty (1997), are discussed. Figure 15(*a*) shows the transverse distributions of the turbulent kinetic energy production term $P = -\langle \bar{\rho} u_i'' u_j'' \rangle \{\tilde{u}_i\}_{,j}$. The production
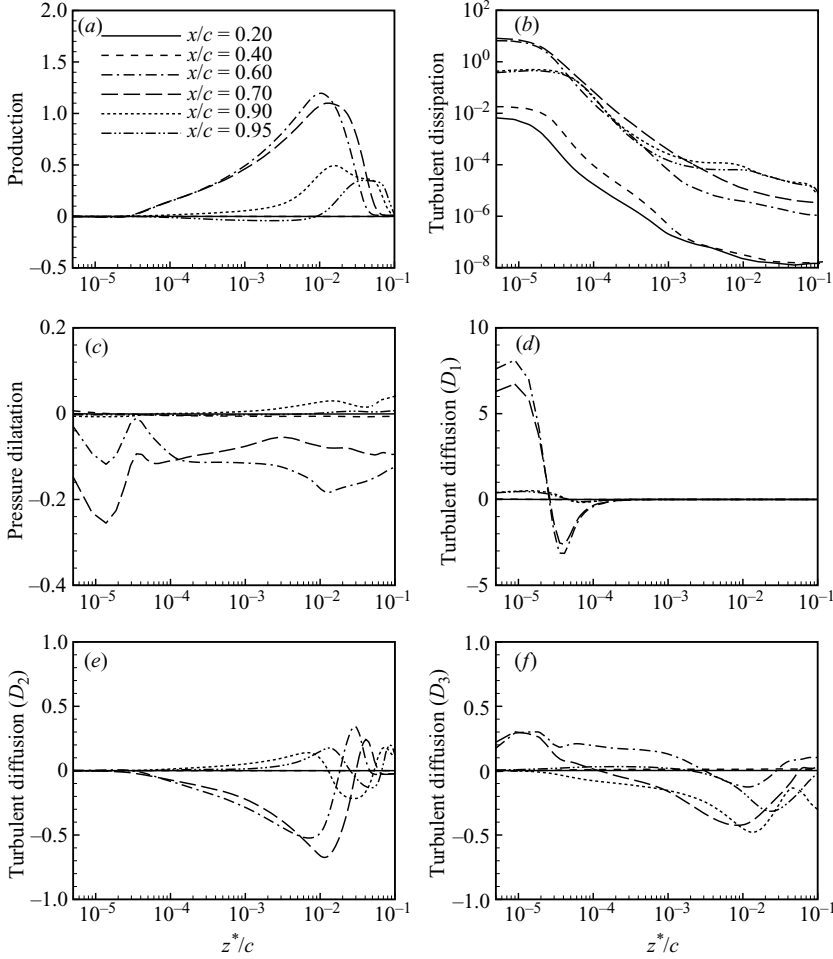
FIGURE 15. Transverse distributions of turbulent kinetic energy budget terms at various streamwise locations: (*a*) turbulent kinetic energy production, (*b*) turbulent dissipation rate, (*c*) pressure dilatation, (*d*) turbulent viscous diffusion, (*e*) turbulent diffusion because of triple velocity correlation and (*f*) turbulent diffusion because of the pressure-velocity correlation.

is very small in region I at for example $x/c = 0.2$ and 0.4, corresponding to the weak turbulent kinetic energy as shown in figure 13. In region II, as the moving shock wave, the production significantly strengthens because of mean velocity gradient. Then, the production in region III gradually decreases, and its peak location corresponds to the strongest shear layer, as seen from the profiles at $x/c = 0.9$ and 0.95.

The profiles of the turbulent dissipation term $\epsilon = \langle \tau''_{ij} u''_{i,j} \rangle$ are shown in figure 15(*b*). The strong dissipation occurs in region II. Similar to the analysis for the near-wall asymptotic behaviour (4.5), turbulent dissipation also obeys the near-wall relation (Patel *et al.* 1985; Speziale *et al.* 1992), i.e. $\epsilon \simeq 2A_k + B_\epsilon z^*$ with B_ϵ being a constant and nearly zero (Pirozzoli & Grasso 2006). It is observed that the profiles follow this relation well in the viscous sublayer shown in figure 15(*b*).

Figure 15(*c*) shows the pressure-dilatation correlation term $T = \langle p' u''_{j,j} \rangle$, which is the net rate of work done by the pressure fluctuations because of the simultaneous fluctuations in dilatation (Sarkar 1992; Lele 1994). This correlation is weak in regions
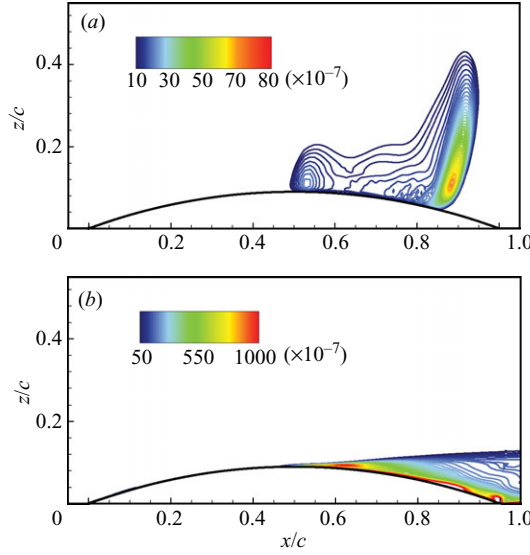
FIGURE 16. Distributions of the turbulent dissipation rate decomposition: (*a*) dilatational part ϵ_d and (*b*) solenoidal part ϵ_s.

I and III, while its distributions around -0.15 appear at $x/c = 0.6$ and 0.7, which are reasonably associated with the shock wave motion and result in turbulence decay because of the compressibility effect.

The turbulent diffusion contains three parts, including the diffusion because of viscous effect $D_1 = \langle \tau_{ij}'' u_i'' \rangle_{,j}$, the triple velocity correlation $D_2 = -\langle \bar{\rho} u_i'' u_i'' u_j''/2 \rangle_{,j}$ and the pressure-velocity correlation $D_3 = -\langle p' u_j'' \rangle_{,j}$, respectively. Their distributions are shown in figures 15(*d*)–15(*f*). The diffusion because of viscous effect plays a dominant role in the viscous sublayer as expected, especially in region II at $x/c = 0.6$ and 0.7 as shown in figure 15(*d*). The turbulent flow undergoes a decay process because of the other two diffusion terms in figures 15(*e*) and 15(*f*). In region III, the turbulent diffusion estimated by the sum of the three parts is mainly responsible for slow decay of turbulence.

We further examine the effect of moving shock wave on the turbulent dissipation rate ϵ, which can be separated into a solenoidal part ϵ_s and a dilatational part ϵ_d (Zeman 1990; Sarkar *et al.* 1991; Lele 1994),

$$\epsilon = \epsilon_s + \epsilon_d = \langle \tau_{ij}'' u_{i,j}'' \rangle$$
$$= \left\langle \frac{\tilde{\mu}}{Re} \omega_i'' \omega_i'' + 2\frac{\tilde{\mu}}{Re} \left(u_{i,j}'' u_{j,i}'' - \left(u_{i,i}'' \right)^2 \right) \right\rangle + \frac{4}{3} \left\langle \frac{\tilde{\mu}}{Re} \left(u_{i,i}'' \right)^2 \right\rangle, \tag{4.6}$$

where ω_i'' denotes the fluctuating vorticity vector. The isocontour lines of both the parts are shown in figure 16. The dilatational part ϵ_d is a pure compressibility effect and obviously occurs in region II in figure 16(*a*), especially around the region in which a series of compression waves coalesce to form a strong shock wave. The solenoidal part ϵ_s is largely independent of the compressibility (Lele 1994) and exists in the near-wall region and in the wake as shown in figure 16(*b*). The dilatational dissipation is enhanced by the moving shock wave at the current Mach number and flow regime, but it remains smaller compared with the total turbulent dissipation rate,
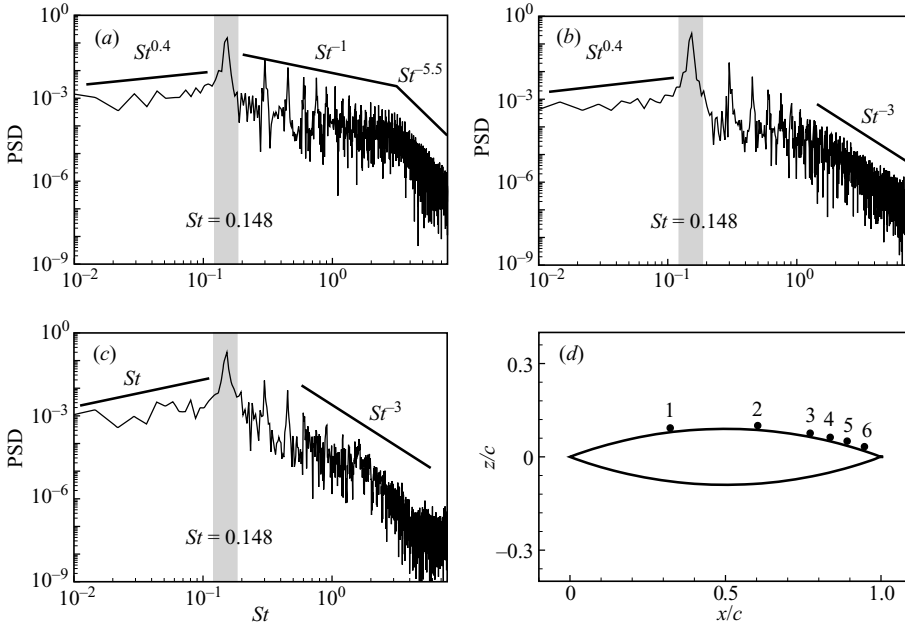
FIGURE 17. Profiles of pressure PSD at various probes: (*a*) probe 1, (*b*) probe 2, (*c*) probe 6 and (*d*) locations of the probes.

consistent with the results of the confined three-dimensional turbulent mixing layer with shocks (Vreman, Kuerten & Geurts 1995).

4.2.6. *Pressure power spectral analysis in turbulent boundary layer*

The pressure power spectral analysis in a turbulent boundary layer is of help in understanding the structure of turbulence (McGrath & Simpson 1987; Simpson, Ghodbane & McGrath 1987; Na & Moin 1998). In addition to the influence of moving shock wave on turbulent boundary layer, the surface curvature related to the pressure gradient is discussed. Figures 17(*a*)–17(*c*) show the profiles of the pressure power spectral density (PSD) at three typical probes 1, 2 and 6 marked in figure 17(*d*), corresponding to regions I, II and III. The profiles of PSD contain a series of peaks including the highest one at $St = 0.148$, associated with the frequency of shock wave motion shown in figure 8, and its harmonics.

The flow in region I is dominated by attached flow with favourable pressure gradient (FPG). It is seen from the profile of PSD in figure 17(*a*) that a nearly flat spectrum with $St^{0.4}$ scaling in lower-frequency regime occurs because of the outer-region velocity and turbulence structure (Panton & Linebarger 1974), while an intermediate frequency range with St^{-1} appears due to the contribution of eddies in the logarithmic region to the wall pressure (Blake 1986). The spectrum collapses at $St = 3$ approximately and varies like $St^{-5.5}$ at higher frequencies caused by the 'active' inner-layer motion (Bradshaw 1967), which is consistent with the measurement performed by McGrath & Simpson (1987) for incompressible attached turbulent boundary layer with FPG.

In region II, the adverse pressure gradient (APG) is strengthened by the upstream-propagating shock and compressible waves from the trailing-edge region. The profile shown in figure 17(*b*) illustrates a flat range with $St^{0.4}$ scaling in the lower-frequency range, has a shorter intermediate region and decays with St^{-3} at higher frequencies,
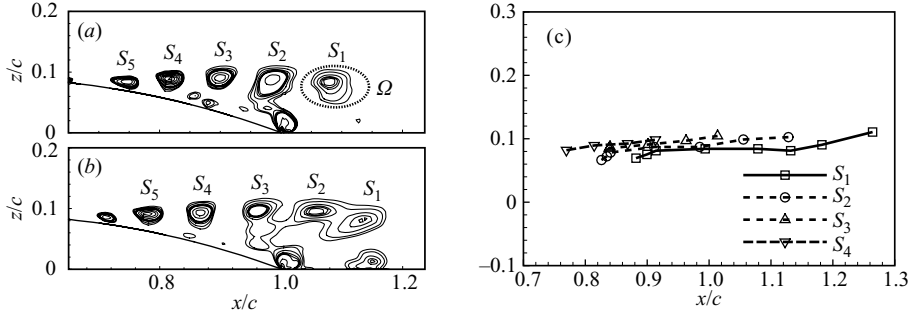
FIGURE 18. Coherent structures educed using isocontours of the Q criterion from 2.5 to $100(U_\infty/c)^2$ at (a) $t^* = 0.5$ and (b) 0.53125; (c) trajectories of the coherent structures.

in agreement with the findings in the strong-APG region of turbulent boundary layer (Simpson *et al.* 1987; Na & Moin 1998).

For the separated turbulent boundary layer, Simpson *et al.* (1987) argued that the pressure spectrum varies as St^1 to $St^{1.4}$ at lower frequencies and decays with St^{-3} scaling at higher frequencies. Similarly, as shown in figure 17(c), the spectrum has St^1 scaling in the low-frequency range and varies approximately like St^{-3} in the higher-frequency range. It should be mentioned that the scaling law at higher frequencies in separated turbulent boundary layer is partly affected by the numerical issue (Na & Moin 1998), and the spectrum normalized by the inner variables may give better collapse (Simpson *et al.* 1987; Na & Moin 1998).

4.3. *Coherent structures and dynamical processes*

4.3.1. *Kinematics of the coherent vortical structures*

The coherent vortical structures educed using the isosurface of the Q criterion (4.1) are shown in figure 6. To clearly exhibit the evolution of the coherent vortical structures, the data are reduced by the spanwise average. Figure 18 shows the isocontour lines of $\langle Q \rangle_s$, where $\langle \ \rangle_s$ denotes the spanwise average. The coherent vortical structures marked by a sequence of S_i ($i = 1$–6) are exhibited. When the structures evolve downstream, their sizes become larger because of the viscous diffusion effect, and the coalescence of the structures also occurs, such as that of S_1 and S_2 in figure 18(b).

The convection speed of the coherent vortical structures is furthermore studied. To identify as rigorously as possible the location of the structures, an approach proposed by Lyn *et al.* (1995) is used, and the location of a structure is determined as

$$(x_s)_i = \frac{\int\int_\Omega x_i(\mathbf{x}) Q_c(\mathbf{x}) \mathrm{d}\Omega}{\int\int_\Omega Q_c(\mathbf{x}) \mathrm{d}\Omega}, \tag{4.7}$$

where Ω is a local integral region containing the vortical structure, as an example for S_1 shown schematically in figure 18(a), and $Q_c = \langle Q \rangle_s \times \mathscr{H}(\langle Q \rangle_s - C_r)$ with $\mathscr{H}$ being the Heaviside distribution. The cutoff value C_r means a threshold of $\langle Q \rangle_s$ (Larchevêque *et al.* 2003) and here is chosen as $(U_\infty/c)^2$. Then, the trajectories of the structures S_i ($i = 1$–4) are given in figure 18(c). Based on the time-dependent location data, the mean convection speed of the coherent vortical structures in the region of $x/c \leqslant 1.2$ can be obtained as approximately $0.35U_\infty$. For comparison, the convection speed of the coherent vortical structures is predicted to be $0.2U_\infty$ for impinging shock
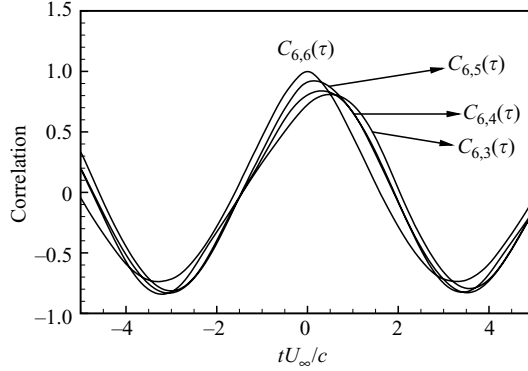
FIGURE 19. Cross-correlation of the downstream-propagating pressure wave.

wave/turbulent boundary layer interaction (Pirozzoli & Grasso 2006) and $0.57U_\infty$ for cavity flow (Heller & Delfs 1996).

Further, we deal with the speed of downstream-propagating pressure waves, which is used in the feedback model of shock wave motion (4.2). Two-point cross-correlation of the unsteady pressure is used to quantitatively determine the propagation speed of the pressure fluctuations along a given path. A covariance coefficient C_{ij} for two pressure signals $p_i(t)$ and $p_j(t)$ with time delay τ can be defined as

$$C_{ij}(\tau) = \frac{\langle (p_i(t) - \langle p_i \rangle_t)(p_j(t-\tau) - \langle p_j \rangle_t) \rangle_t}{\langle (p_i(t) - \langle p_i \rangle_t)^2 (p_j(t) - \langle p_j \rangle_t)^2 \rangle_t}, \tag{4.8}$$

where $\langle\ \rangle_t$ denotes time average. Within the separation region, the cross-correlation analysis is conducted for probes 3–6 shown in figure 17(d), and the results are exhibited in figure 19. The positive time delays are obtained, indicating that the pressure disturbances within the separated region behind the shock wave propagate downstream towards the aerofoil trailing edge. The local propagation speed of the pressure disturbances can be calculated by dividing the spatial distances between the neighbouring probes by the time delays between the peaks of the corresponding cross-correlations (Xiao *et al.* 2006). Then, the speed is determined as approximately $0.34U_\infty$, consistent with the convection speed of the coherent vortical structures, $0.35U_\infty$, given above.

4.3.2. *Dynamical processes in flow evolution*

To reveal the dynamical processes, the Lamb vector divergence and curl, which are associated with the momentum and vorticity transport in flow field (Wu *et al.* 2006; Hamman *et al.* 2008), are discussed. To simplify the post-process and clearly present the flow structures, the Lamb vector divergence and curl are calculated using the spanwise-averaged velocity and shown in figure 20.

As shown in figures 20(a) and 20(b) for the distributions of the Lamb vector divergence, two-layer structures with signs opposite of that of the Lamb vector divergence, corresponding to the separated shear layer induced by shock wave, are observed on the upper surface. Based on the analysis of the Lamb vector divergence (Hamman *et al.* 2008), both the negative and positive values represent vorticity-bearing motions and straining motions, respectively. As a result, the dynamical processes in the two layers include that the interaction between the strong strain rate region and strong vorticity region may exchange the momentum. The Lamb vector divergence
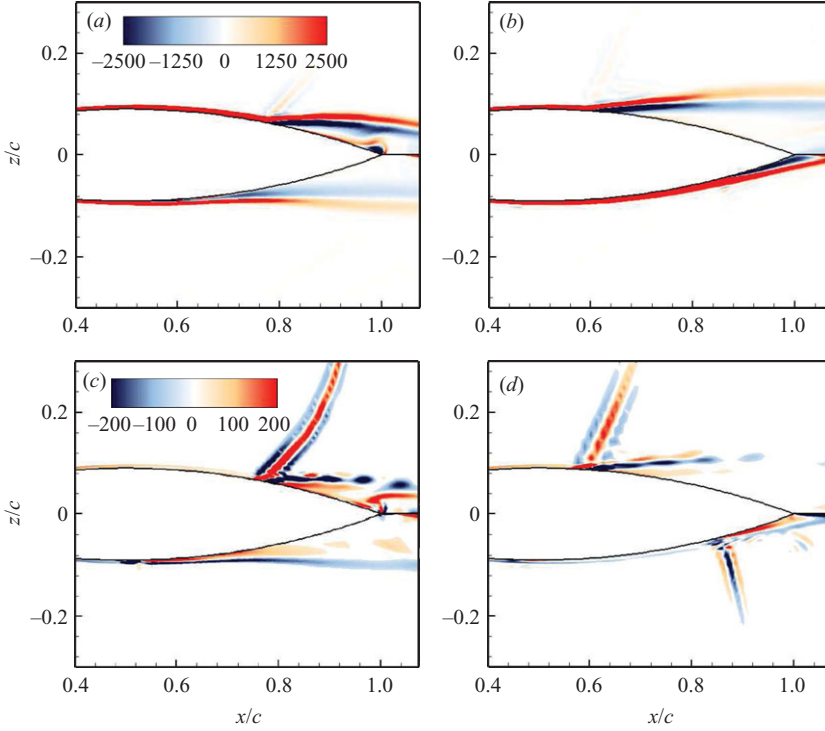
FIGURE 20. Distributions of the Lamb vector divergence at (*a*) $t^* = 0.5$ and (*b*) $t^* = 0.625$ and of the Lamb vector curl at (*c*) $t^* = 0.5$ and (*d*) $t^* = 0.625$.

reasonably captures the temporal evolution of high- and low-momentum fluid flow, which is closely associated with the mechanisms that drive turbulent shear layer evolution separated from the aerofoil surface.

The distributions of the Lamb vector divergence apparently exhibit large magnitude in turbulent shear layer region and relatively small magnitude in shock wave region in figures 20(*a*) and 20(*b*). Moreover, the Lamb vector divergence appears as an acoustic source term in Lighthill's wave equation (Lighthill 1952; Howe 1975). Thus, the acoustic character is mainly handled by turbulent shear layer evolution near the trailing edge of the aerofoil, consistent with the previous flow-noise prediction on turbulent boundary layers (Wang & Moin 2000; Wang *et al.* 2006). Based on the theoretical prediction of LIA on the acoustic wave generation behind the shock wave (Ribner 1953, 1954), the moving shock wave strengthens turbulent shear layers and then affects the acoustic character from the distributions of the Lamb vector divergence in figures 20(*a*) and 20(*b*).

The distributions of the Lamb vector curl are correspondingly shown in figures 20(*c*) and 20(*d*). Three-layer structures along curving shock wave are illustrated in the shock wave region, while the shock wave structure is hardly identified by the Lamb vector divergence as shown in figures 20(*a*) and 20(*b*). On the upper surface, the bead-like structures with negative values of the Lamb vector curl along the separated shear layer in figure 20(*c*) correspond reasonably with the coherent vortical structures in figure 18(*a*). The Lamb vector curl is directly related to the vorticity transport (Wu *et al.* 2006). Based on the analysis of the terms in the vorticity transport equation (not shown here), we have identified that the captured three-layer structures along the

curving shock wave are mainly associated with the convection process with additional contribution of the dilatation effect to the mid-layer.

4.3.3. *Proper orthogonal decomposition analysis of the pressure field*

The pressure field can be quantitatively analysed using the POD method to extract energetic coherent structures from the simulation data. For a given pressure field $p(\boldsymbol{x}, t)$, the POD analysis can determine a set of orthogonal functions $\phi_j(\boldsymbol{x})$, $j = 1, 2, \ldots$, so that projection of p on to the first n functions,

$$\hat{p}(\boldsymbol{x}, t) = \bar{p}(\boldsymbol{x}, t) + \sum_{j=1}^{n} a_j(t)\phi_j(\boldsymbol{x}), \tag{4.9}$$

has the smallest error, defined as $\langle \|p - \hat{p}\|^2 \rangle_t$, where $\langle\ \rangle_t$ and $\|\cdot\|$ denote the time average and a norm in the L^2 space, respectively. Here, $a_j(t)$ represents the temporal variation of the jth mode. A more complete discussion of this subject can be found in Berkooz *et al.* (1993).

The analysis has been conducted using $N_t = 500$ snapshots of the spanwise-averaged pressure fields spanning a time period of $102.39c/U_\infty$, and the temporal resolution is $0.21c/U_\infty$, corresponding to a cutoff Strouhal number about 2.44. The energy of the jth mode, E_j, is defined as

$$E_j = \langle \|a_j(t)\phi_j(\boldsymbol{x})\|^2 \rangle_t. \tag{4.10}$$

The normalized energy of the mth mode is then defined as $E_m / \sum_{j=1}^{N_t} E_j$, and the energy sum from mode 1 through to mode m is solved as $\sum_{j=1}^{m} E_j / \sum_{j=1}^{N_t} E_j$.

Using the time-varying coefficient $a_j(t)$ in (4.9), one can obtain the frequency spectrum of the jth mode and the phase difference from the adjacent modes (Wang, Hsieh & Yang 2005). The shape distributions and corresponding frequency spectra of the first six modes are shown in figure 21.

The first two modes account for more than 81 % of the total energy of the fluctuating pressure fields and exhibit asymmetric shapes in figure 21(*a*). The dominant frequency of the first two modes is $St_{1,2} = 0.148$, shown in their spectra as expected, and the phase difference between them is $\pi/2$. These two modes are associated with the moving shock waves and their induced separated shear layers, consistent with the fact that the flow structures are dominated by the alternately moving shock waves along the upper and lower sides of the aerofoil (Bourguet, Braza & Dervieux 2007).

The shapes of the third and fourth modes appear symmetric in figure 21(*b*). These two modes occupy about 10 % of the total energy with $\pi/2$ phase difference, and the dominant frequency is $St_{3,4} = 0.296$ with its harmonic frequency 0.592 exhibited in the spectrum. The shapes in the wake are similar to the ones of the flow structures behind a circular cylinder (Deane *et al.* 1991). It is reasonably identified that these modes may be related to the wake flow behind the aerofoil. Further, it is examined that both the fifth and the sixth mode only contain about 3 % of the total energy with the shapes shown in figure 21(*c*). Spectral peaks occur in linear combinations of the frequencies in the former modes, i.e. $St_{1,2} + St_{3,4} = 0.444$ and $St_{1,2} + 2St_{3,4} = 0.740$, because of the interaction of the former modes.

Based on the POD analysis, we can reasonably identify that the first two modes play a dominant role in the evolution of pressure field and associate with the moving shock waves and the separated shear layers in the trailing-edge region, consistent with the distributions of the Lamb vector divergence in figures 20(*a*) and 20(*b*). The results
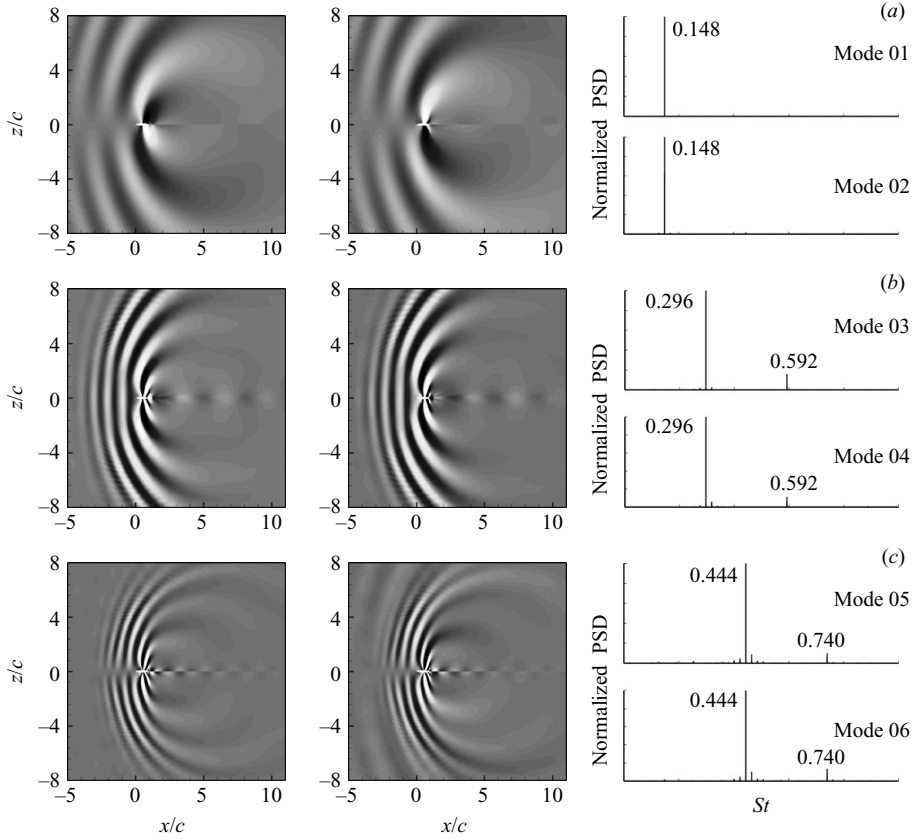
FIGURE 21. Spatial distributions of first six POD modes and power spectra of their time-varying coefficients: (*a*) modes 1 and 2 (levels between −1.0 and $1.0\rho_\infty U_\infty^2$) and their spectra; (*b*) modes 3 and 4 (levels between −0.2 and $0.2\rho_\infty U_\infty^2$) and their spectra; (*c*) modes 5 and 6 (levels between −0.2 and $0.2\rho_\infty U_\infty^2$) and their spectra.

obtained are of help in understanding the physical mechanisms of the flow-generated sound involved in this flow.

5. Concluding remarks

Numerical investigation on the compressible flow past an aerofoil was carried out by means of a DES technique. Various fundamental mechanisms dictating the complex flow behaviours, including moving shock wave evolution, turbulent boundary layer characteristics and coherent structures and dynamical processes, were examined systematically and are summarized briefly as follows.

Self-sustained shock wave motions repeated alternately along the upper and lower surfaces of the aerofoil are reasonably identified, which belong to type C as classified by Tijdeman & Seebass (1980) and agree with the previous experimental findings (McDevitt *et al.* 1976; Levy 1978; McDevitt 1979; Marvin *et al.* 1980). In particular, based on the feedback mechanism of self-sustained shock oscillation proposed by Lee (1990), a feedback model is developed to extendedly describe the present type C shock motion, and the frequency of the feedback loop predicted by this

model agrees well with those obtained by the previous experiments and the present calculation.

As the substantial unsteadiness of moving shock wave on the aerofoil, we may classify three typical flow regimes, namely attached boundary layer, moving shock wave/turbulent boundary layer interaction and intermittent boundary layer separation region. Turbulent boundary layer characteristics in terms of mean velocity, turbulence intensities, turbulent kinetic energy, pressure power spectra and the relevant turbulent quantities have been analysed in detail in the three flow regions. The turbulence intensities are significantly enhanced with a strengthened turbulent kinetic energy production induced by the moving shock wave. The pressure-dilatation correlation term related to the compressibility effect is relatively important in the shock wave/boundary layer interaction region and reasonably makes turbulence decay. Moreover, as the turbulent dissipation rate can be separated into solenoidal and dilatational parts, it is identified that the dilatational dissipation is enhanced by the moving shock wave but remains smaller, and the solenoidal dissipation exists mainly in the near-wall region and in the wake. In addition, the pressure power spectral analysis exhibits that there exist different spectral scalings with the frequency in the three flow regions.

The kinematics of the coherent vortical structures are analysed using the Q criterion and two-point cross-correlation approach. The speed of downstream-propagating pressure waves in the separated boundary layer is obtained and is found to be consistent with the convection speed of the coherent vortical structures. Moreover, the dynamical processes in flow evolution are discussed based on the instantaneous Lamb vector divergence and curl. The Lamb vector divergence reasonably captures the temporal evolution of high- and low-momentum fluid flow with two-layer structures in the separated shear layer, closely related to the mechanisms that drive turbulent shear layer evolution separated from the aerofoil surface. The Lamb vector curl clearly identifies three-layer structures along the curving shock wave, which are mainly associated with the convection process with additional contribution of the dilatation effect to the mid-layer. Further, the POD analysis of the pressure field is also performed to extract energetic coherent structures. The dominated modes are associated with the moving shock waves and the separated shear layers in the trailing-edge region, consistent with the distribution of the Lamb vector divergence which appears as an acoustic source term in Lighthill's wave equation.

REFERENCES

ADRIAN, R. J. & MOIN, P. 1988 Stochastic estimation of organized turbulent structure: homogeneous shear flow. *J. Fluid Mech.* **190**, 531–559.

ANDREOPOULOS, Y., AGUI, J. H. & BRIASSULIS, G. 2000 Shock wave-turbulence interactions. *Annu. Rev. Fluid Mech.* **32**, 309–345.

BERKOOZ, G., HOLMES, P. & LUMLEY, J. L. 1993 The proper orthogonal decomposition in the analysis of turbulent flows. *Annu. Rev. Fluid Mech.* **25**, 539–575.

BLAKE, W. K. 1986 *Mechanics of Flow-Induced Sound and Vibration II*. Academic.

BOURGUET, R., BRAZA, M. & DERVIEUX, A. 2007 Reduced-order modelling for unsteady transonic flows around an airfoil. *Phys. Fluids* **19**, 111701.

BRADSHAW, P. 1967 The turbulence structure of equilibrium boundary layers. *J. Fluid Mech.* **29**, 625–645.

BRADSHAW, P. 1977 Compressible turbulent shear layers. *Annu. Rev. Fluid Mech.* **9**, 33–54.

CHAKRABORTY, P., BALACHANDAR, S. & ADRIAN, R. J. 2005 On the relationships between local vortex identification schemes. *J. Fluid Mech.* **535**, 189–214.

CROUCH, J. D., GARBARUK, A. & MAGIDOV, D. 2007 Predicting the onset of flow unsteadiness based on global instability. *J. Comput. Phys.* **224**, 924–940.

CROUCH, J. D., GARBARUK, A., MAGIDOV, D. & TRAVIN, A. 2009 Origin of transonic buffet on aerofoils. *J. Fluid Mech.* **628**, 357–369.

DEANE, A. E., KEVREKIDIS, I. G., KARNIADAKIS, G. E. & ORSZAG, S. A. 1991 Low-dimensional models for complex geometry flows: application to grooved channels and circular cylinders. *Phys. Fluids* A **3**, 2337–2354.

DECK, S. 2005 Numerical simulation of transonic buffet over a supercritical airfoil. *AIAA J.* **43**, 1556–1566.

GARNIER, E., SAGAUT, P. & DEVILLE, M. 2002 Large eddy simulation of shock/homogeneous turbulence interaction. *Comput. Fluids* **31**, 245–268.

GIRARD, S. 1999 Etude des Charges Latérales dans une Tuyére Supersonique Surdétendue. PhD thesis, Université de Poitiers, Poitiers, France.

HAMMAN, C. W., KLEWICKI, J. C. & KIRBY, R. M. 2008 On the Lamb vector divergence in Navier–Stokes flows. *J. Fluid Mech.* **610**, 261–284.

HARSHA, P. T. & LEE, S. C. 1970 Correlation between turbulent shear stress and turbulent kinetic energy. *AIAA J.* **8**, 1508–1510.

HELLER, H. & DELFS, J. 1996 Cavity pressure oscillations: the generating mechanism visualized. *J. Sound Vib.* **196**, 248–252.

HERRIN, J. L. & DUTTON, J. C. 1997 The turbulence structure of a reattaching axisymmetric compressible free shear layer. *Phys. Fluids* **9**, 3502–3512.

HILL, D. J., PANTANO, C. & PULLIN, D. I. 2006 Large-eddy simulation and multiscale modelling of a Richtmyer–Meshkov instability with reshock. *J. Fluid Mech.* **557**, 29–61.

HO, C. M. & NOSSEIR, N. S. 1981 Dynamics of an impinging jet. Part 1. The feedback phenomenon. *J. Fluid Mech.* **105**, 119–142.

HOWE, M. S. 1975 Contributions to the theory of aerodynamic sound, with application to excess jet noise and the theory of the flute. *J. Fluid Mech.* **71**, 625–673.

JACQUIN, L., CAMBON, C. & BLIN, E. 1993 Turbulence amplification by a shock wave and rapid distortion theory. *Phys. Fluids* A **5**, 2539–2550.

JEONG, J. & HUSSAIN, F. 1995 On the identification of a vortex. *J. Fluid Mech.* **285**, 69–94.

KAWAI, S. & FUJII, K. 2005 Computational study of supersonic base flow using hybrid turbulence methodology. *AIAA J.* **43**, 1265–1275.

LARCHEVÊQUE, L., SAGAUT, P., MARY, I. & LABBÉ, O. 2003 Large-eddy simulation of a compressible flow past a deep cavity. *Phys. Fluids* **15**, 193–210.

LEE, B. H. K. 1990 Oscillatory shock motion caused by transonic shock boundary-layer interaction. *AIAA J.* **28**, 942–944.

LEE, B. H. K. 2001 Self-sustained shock oscillations on airfoils at transonic speeds. *Prog. Aerosp. Sci.* **37**, 147–196.

LEE, B. H. K., MURTY, H. & JIANG, H. 1994 Role of Kutta waves on oscillatory shock motion on an airfoil. *AIAA J.* **32**, 789–796.

LEE, S., LELE, S. K. & MOIN, P. 1997 Interaction of isotropic turbulence with shock waves: effect of shock strength. *J. Fluid Mech.* **340**, 225–247.

LELE, S. K. 1992 Shock-jump relations in a turbulent flow. *Phys. Fluid* A **4**, 2900–2905.

LELE, S. K. 1994 Compressibility effects on turbulence. *Annu. Rev. Fluid Mech.* **26**, 211–254.

LEVY, L. L. 1978 Experimental and computational steady and unsteady transonic flows about a thick airfoil. *AIAA J.* **16**, 564–572.

LIGHTHILL, M. J. 1952 On sound generated aerodynamically. Part I. General theory. *Proc. R. Soc. Lond.* A **211**, 564–587.

LOGINOV, M. S., ADAMS, N. A. & ZHELTOVODOV, A. A. 2006 Large-eddy simulation of shock-wave/turbulent-boundary-layer interaction. *J. Fluid Mech.* **565**, 135–169.

Lu, X. Y., Wang, S. W., Sung, H. G., Hsieh, S. Y. & Yang, V. 2005 Large-eddy simulations of turbulent swirling flows injected into a bump chamber. *J. Fluid Mech.* **527**, 171–195.

Lumley, J. L. 1967 Rational approach to relations between motions of differing scales in turbulent flows. *Phys. Fluids* **10**, 1405–1408.

Lyn, D. A., Einav, S., Rodi, W. & Park, J.-H. 1995 A laser-Doppler velocimetry study of ensemble-averaged characteristics of the turbulent near wake of a square cylinder. *J. Fluid Mech.* **304**, 285–319.

Marvin, J. G., Levy, L. L. & Seegmiller, H. L. 1980 Turbulence modelling for unsteady transonic flows. *AIAA J.* **18**, 489–496.

Mary, I. & Sagaut, P. 2002 Large eddy simulation of flow around an airfoil near stall. *AIAA J.* **40**, 1139–1145.

McDevitt, J. B. 1979 Supercritical flow about a thick circular-arc airfoil. *NASA Tech. Mem.* 78549.

McDevitt, J. B., Levy, L. L. & Deiwert, G. S. 1976 Transonic flow about a thick circular-arc airfoil. *AIAA J.* **14**, 606–613.

McGrath, B. E. & Simpson, R. L. 1987 Some features of surface pressure fluctuations in turbulent boundary layers with zero and favourable pressure gradients. *Tech Rep.* NASA CR-4051. NASA.

Na, Y. & Moin, P. 1998 The structure of wall-pressure fluctuations in turbulent boundary layers with adverse pressure gradient and separation. *J. Fluid Mech.* **377**, 347–373.

Nikitin, N. V., Nicoud, F., Wasistho, B., Squires, K. D. & Spalart, P. R. 2000 An approach to wall modelling in large-eddy simulations. *Phys. Fluids* **12**, 1629–1632.

Panton, R. L. & Linebarger, J. H. 1974 Wall pressure spectra calculations for equilibrium boundary layers. *J. Fluid Mech.* **65**, 261–287.

Patel, V. C., Rodi, W. & Scheuerer, G. 1985 Turbulence models for near-wall and low Reynolds number flows: a review. *AIAA J.* **23**, 1308–1319.

Pirozzoli, S. & Grasso, F. 2006 Direct numerical simulation of impinging shock wave/turbulent boundary layer interaction at $M = 2.25$. *Phys. Fluids* **18**, 065113.

Pope, S. B. 2000 *Turbulent Flows*. Cambridge University Press.

Ribner, H. S. 1953 Convection of a pattern of vorticity through a shock wave. *Tech Rep.* NACA TN-2864. NACA.

Ribner, H. S. 1954 Shock-turbulence interaction and the generation of noise. *Tech Rep.* NACA TN-3255. NACA

Ribner, H. S. 1987 Spectra of noise and amplified turbulence emanating from shock-turbulence interaction. *AIAA J.* **25**, 436–442.

Ringuette, M. J., Wu, M. & Martín, M. P. 2008 Coherent structures in direct numerical simulation of turbulent boundary layers at Mach 3. *J. Fluid Mech.* **594**, 59–69.

Robinson, S. K. 1991 Coherent motions in the turbulent boundary layers. *Annu. Rev. Fluid Mech.* **23**, 601–639.

Rumsey, C. L., Sanetrik, M. D., Biedron, R. T., Melson, N. D. & Parlette, E. B. 1996 Efficiency and accuracy of time-accurate turbulent Navier–Stokes computations. *Comput. Fluids* **25**, 217–236.

Sagaut, P. 2002 *Large-Eddy Simulation for Incompressible Flows*. Springer.

Sagaut, P., Deck, S. & Terracol, M. 2006 *Multiscale and Multiresolution Approaches in Turbulence*. Imperial College Press.

Sarkar, S. 1992 The pressure-dilatation correlation in compressible flows. *Phys. Fluids* A **4**, 2674–2682.

Sarkar, S., Erlebacher, G., Hussaini, M. Y. & Kreiss, H. O. 1991 The analysis and modelling of dilatational terms in compressible turbulence. *J. Fluid Mech.* **227**, 473–493.

Shur, M. L., Spalart, P. R., Strelets, M. & Travin, A. 1999 Detached-eddy simulation of an airfoil at high angle of attack. In *Fourth International Symposium on Engineering Turbulence Modelling and Measurements* (ed. W. Rodi & D. Laurence) pp. 669–678. Elsevier.

Shyy, W. & Krishnamurty, V. S. 1997 Compressible effects in modelling complex turbulent flows. *Prog. Aerosp. Sci.* **33**, 587–645.

Simon, F., Deck, S., Guillen, P., Sagaut, P. & Merlen, A. 2007 Numerical simulation of the compressible mixing layer past an axisymmetric trailing edge. *J. Fluid Mech.* **591**, 215–253.

Simpson, R. L., Ghodbane, M. & McGrath, B. E. 1987 Surface pressure fluctuations in a separating turbulent boundary layer. *J. Fluid Mech.* **177**, 167–186.

SMITS, A. J. & DUSSAUGE, J. P. 1996 *Turbulent Shear Layers in Supersonic Flow*. American Institute of Physics.

SPALART, P. R. 2001 Young-person's guide to detached eddy simulation grids. *Tech Rep.* NACA CR-2001 211032. NACA.

SPALART, P. R. 2009 Detached-eddy simulation. *Annu. Rev. Fluid Mech.* **41**, 181–202.

SPALART, P. R. & ALLMARAS, S. R. 1992 A one-equation turbulence model for aerodynamic flows. *AIAA paper* 92-0439. AIAA.

SPALART, P. R., JOU, W. H., STRELETS, M. & ALLMARAS, S. R. 1997 Comments on the feasibility of LES for wings and on a hybrid RANS/LES approach. In *Proceedings of the First AFOSR International Conference on DNS/LES*, Ruston, LA.

SPEZIALE, C. G., ABID, R. & ANDERSON, E. C. 1992 Critical evaluation of two-equation models for near-wall turbulence. *AIAA J.* **30**, 324–331.

TERAMOTO, S. 2005 Large-eddy simulation of transitional boundary layer with impinging shock wave. *AIAA J.* **43**, 2354–2363.

TIJDEMAN, H. 1977 Investigation of the transonic flow around oscillating airfoils. *Tech Rep.* NLR TR 77090U. National Aerospace Laboratory, The Netherlands.

TIJDEMAN, H. & SEEBASS, R. 1980 Transonic flow past oscillating airfoils. *Annu. Rev. Fluid Mech.* **12**, 181–222.

TRUESDELL, C. 1954 *The Kinematics of Vorticity*. Indiana University Press.

VREMAN, B., KUERTEN, H. & GEURTS, B. 1995 Shocks in direct numerical simulation of the confined three-dimensional mixing layer. *Phys. Fluids* **7**, 2105–2107.

WANG, M., FREUND, J. B. & LELE, S. K. 2006 Computational prediction of flow-generated sound. *Annu. Rev. Fluid Mech.* **38**, 483–512.

WANG, M. & MOIN, P. 2000 Computation of trailing-edge flow and noise using large-eddy simulation. *AIAA J.* **38**, 2201–2209.

WANG, S. W., HSIEH, S. Y. & YANG, V. 2005 Unsteady flow evolution in swirl injector with radial entry. Part I. Stationary conditions. *Phys. Fluids* **17**, 045106.

WANG, S. W., YANG, V., HSIAO, G., HSIEH, S. Y. & MONGIA, H. C. 2007 Large-eddy simulations of gas-turbine swirl injector flow dynamics. *J. Fluid Mech.* **583**, 99–122.

WU, J. Z., MA, H. Y. & ZHOU, M. D. 2006 *Vorticity and Vortex Dynamics*. Springer.

XIAO, Q., TSAI, H. M. & LIU, F. 2003 Computation of shock induced separated flow with a lagged k–ω turbulence model. *AIAA paper* 2003-3464. AIAA.

XIAO, Q., TSAI, H. M. & LIU, F. 2006 Numerical study of transonic buffet on a supercritical airfoil. *AIAA J.* **44**, 620–628.

XU, C. Y., CHEN, L. W. & LU, X. Y. 2009 Numerical investigation of shock wave and turbulence interaction over a circular cylinder. *Mod. Phys. Lett.* B **23**, 233–236.

ZEMAN, O. 1990 Dilatation dissipation: the concept and application in modelling compressible mixing layers. *Phys. Fluids* A **2**, 178–188.